

# A CHANDRA ARCHIVAL STUDY OF THE TEMPERATURE AND METAL ABUNDANCE PROFILES IN HOT GALAXY CLUSTERS AT $0.1 \lesssim Z \lesssim 0.3$

A. BALDI

Harvard-Smithsonian Center for Astrophysics

S. ETTORI

INAF - Osservatorio Astronomico di Bologna

P. MAZZOTTA<sup>1</sup>

Università di Roma "Tor Vergata", Dip. di Fisica

P. TOZZI<sup>2</sup>

INAF - Osservatorio Astronomico di Trieste

S. BORGANI<sup>2,3</sup>

Dipartimento di Astronomia dell'Università di Trieste

*Accepted by the Astrophysical Journal*

## ABSTRACT

We present the analysis of the temperature and metallicity profiles of 12 galaxy clusters in the redshift range 0.1–0.3 selected from the Chandra archive with at least  $\sim 20,000$  net ACIS counts and  $kT > 6$  keV. We divide the sample between 7 Cooling-Core (CC) and 5 Non-Cooling-Core (NCC) clusters according to their central cooling time. We find that single power-laws can describe properly both the temperature and metallicity profiles at radii larger than  $0.1r_{180}$  in both CC and NCC systems, showing the NCC objects steeper profiles outwards. A significant deviation is only present in the inner  $0.1r_{180}$ . We perform a comparison of our sample with the De Grandi & Molendi BeppoSAX sample of local CC and NCC clusters, finding a complete agreement in the CC cluster profile and a marginally higher value (at  $\sim 1\sigma$ ) in the inner regions of the NCC clusters. The slope of the power-law describing  $kT(r)$  within  $0.1r_{180}$  correlates strongly with the ratio between the cooling time and the age of the Universe at the cluster redshift, being the slope  $> 0$  and  $\tau_c/\tau_{age} \lesssim 0.6$  in CC systems.

*Subject headings:* galaxies: clusters: general — (galaxies:) intergalactic medium — X-rays: galaxies: clusters

## 1. INTRODUCTION

Clusters of galaxies represent unique signposts in the Universe, where the physical properties of the cosmic diffuse baryons can be studied in great details and used to trace the past history of cosmic structure formation (e.g. Rosati et al. 2002; Voit 2005, for reviews). As a result of adiabatic compression and shocks generated by supersonic motion during shell crossing and virialization, a hot thin gas permeating the cluster gravitational potential well is formed. Typically this gas, which is enriched with metals ejected from supernovae (SNe) explosions through subsequent episodes of star formation (e.g. Matteucci & Vettolani 1988; Renzini 1997), reaches temperatures of several  $10^7$  K and therefore emits mainly via thermal bremsstrahlung in the X-rays. At such temperatures most of the elements are either fully ionized or in a high ionization state.

Particularly evident in X-ray spectra of galaxy clusters are the strong transitions to the  $n = 1$  level (K-shell) of the H-like and He-like ions of Iron in the energy range

6.7–6.9 keV. Below 2 keV,  $n = 2$  level (L-shell) transition of Iron and  $\alpha$  elements can be detected, especially in the low temperature region in the centers of the so-called cool core clusters, that are characterized by a strong peak in the surface brightness distribution, and therefore short cooling times. Spatially resolved CC clusters show a peak in the metal distribution associated to the low temperature core region (e.g. De Grandi & Molendi 2001 and 2002, hereafter DM01 and DM02). Although the amount of energy supplied to the intra-cluster medium (ICM) by SNe explosions depends on several factors (e.g. the physical condition of the ICM at the epoch of the enrichment) and cannot be obtained directly from X-ray observations, the radial distribution of metals, as well as their abundance as a function of time, are crucial information to shed light on the cosmic star formation history and to trace the effect of SN feedback on the ICM.

Several analyses have been presented in the literature with the aim to study the radial distribution of metals in clusters of galaxies. Finoguenov, David & Ponman (2000) performed a spatially resolved X-ray spectroscopic analysis of 11 relaxed clusters observed by ROSAT and ASCA, deriving a radial distribution of single heavy elements such as Fe, Si, Ne and S. They found that the to-

<sup>1</sup> Harvard-Smithsonian Center for Astrophysics

<sup>2</sup> INFN - Sezione di Trieste

<sup>3</sup> INAF - Osservatorio Astronomico di Trieste

tal Fe abundance decreases significantly with radius in all clusters, while the Si, Ne and S abundances are either flat or decrease less rapidly. DM01 derived radial metallicity profiles (mainly driven by Fe) of 17 nearby clusters observed by BeppoSAX. They found a strong enhancement in the abundance in the central regions of the CC clusters. A flatter metallicity profile was observed instead for the non-cool core clusters in their sample. Since all the NCC clusters show signs of recent merger activity, they suggested that the merger events may have redistributed efficiently the metal content of the intracluster medium. Irwin & Bregman (2001) derived iron-abundance profiles for 12 clusters with  $0.03 \leq z \leq 0.2$  observed by Beppo SAX. Although they investigated the differences between CC and NCC clusters in a less systematic way than DM01, they found a negative gradient in the abundance profiles of all the CC clusters and to a lesser significance also in the NCC clusters. Similarly to DM01, they found that CC clusters have higher metallicity than NCC clusters at every radius. It is worth to say that the aforementioned papers investigated the metallicity trends only within  $r_{500}$ . Spatially resolved measures of the metal abundance in galaxy clusters were performed also with XMM-Newton. In particular Tamura et al. (2004) analyzed a sample of 19 X-ray bright relaxed clusters, obtaining elemental abundances of Fe, Si, S and O. They found that while the distribution of Fe, Si and S is generally peaked toward the center, the O abundances are uniform throughout the cluster, pointing out to a different origin among these metals, most likely in SNe Ia and II. More recently Vikhlinin et al. (2005) have derived temperature and metallicity profiles for 11 low-redshift clusters observed by Chandra. The clusters in their sample however are all CC clusters, presenting a very regular overall X-ray morphology and showing only very weak signs of dynamical activity. Although they have not analyzed the metallicity profiles rescaled to the virial radius of the cluster (as they did for the temperature profiles) a negative gradient of  $Z$  is present in all the objects in their sample. However, almost all the spatially-resolved metallicity profiles are measured in local clusters ( $z < 0.1$ ).

On the other hand, measurements of the metal content of the intracluster medium at high- $z$  has been obtained with single emission-weighted estimates from Chandra and XMM-Newton exposures of 56 clusters at  $0.3 \lesssim z \lesssim 1.3$  in Balestra et al. (2007). They measured the Iron abundance within  $(0.15-0.3)R_{vir}$  and found a negative evolution of  $Z_{Fe}$  with the redshift, with clusters at  $z \gtrsim 0.5$  having a constant average Fe abundance of  $\approx 0.25Z_{\odot}$ , while objects in the redshift range  $0.3 \lesssim z \lesssim 0.5$  show  $Z_{Fe}$  significantly higher ( $\approx 0.4Z_{\odot}$ ). Such evolution is not driven entirely by the presence of the cool cores. This result has been recently confirmed by Maughan et al. (2007).

In this paper, we present measurements of the radial temperature and metallicity profiles of a sample of 12 clusters with temperatures larger than 6 keV observed with Chandra at intermediate redshift,  $0.11 \leq z \leq 0.32$ . We take advantage of the ACIS superior spatial and spectral resolution to investigate in a systematic fashion the differences that may exist between CC and NCC clusters. The spectroscopic measurements of the ICM temperature and metallicity allow to characterize statistically the radial profiles and to quantify their gradients in

this unexplored redshift region.

All the uncertainties are quoted at  $1\sigma$  (68%) for one interesting parameter. The abundance estimates are relative to the compilation of cosmic values given in Anders & Grevesse (1989) (hereafter AG89), unless otherwise stated. Indeed, these values for the solar metallicities have more recently been superseded by the new values by Grevesse & Sauval (1998) and Asplund et al. (2005) (hereafter A05), who introduced a 0.676 and 0.60 times lower Iron solar abundance, respectively (photospheric value), while the other elements do not change significantly. Our measures of metallicity are expected to be driven mainly by Iron, however, for clarity, we also performed the fits using solar abundances by A05. Throughout this paper we assume  $H_0 = 100 h \text{ km s}^{-1} \text{ Mpc}^{-1}$ ,  $h = 0.7$ ,  $\Omega_m = 0.3$  and  $\Omega_{\Lambda} = 0.7$ .

## 2. SAMPLE DEFINITION AND DATA ANALYSIS

From Chandra archival data we select a sample of twelve ‘intermediate’ redshift clusters ( $0.11 \leq z \leq 0.32$ ). We also require the clusters to have at least  $\sim 20,000$  ACIS-S or ACIS-I counts in order to study their properties in at least 3 circular annuli. The sample is presented in Table 1, where the name of the cluster and the Chandra observing logs are listed.

The Chandra data analysis has been performed using the latest version of CIAO (v3.3.0.1). All of our datasets are processed by a version of the Standard Data Processing (SDP) pipeline prior to version DS 7.4.0, which uses the tool *acis\_detect\_afterglow* to flag possible cosmic ray events in the level 1 event file; it has been determined that a significant fraction of the X-ray events from a source in imaging mode might be removed using this tool. Therefore we reset the correction performed by *acis\_detect\_afterglow* on the Level=1 event file, so that the hot pixels and the afterglow events may be properly removed by the improved CIAO tool *acis\_run\_hotpix*, (introduced after SDP version DS 7.4.0). A new Level=1 event file is then created (through the CIAO tool *acis\_process\_events*) to apply the latest calibration files to the data (e.g. apply the newest ACIS gain maps, apply the time-dependent ACIS gain correction, apply the ACIS Charge Transfer Inefficiency correction, etc.). Moreover in the case of observations telemetered in VFaint mode it is possible to reduce the background using the additional screening of the events with significantly positive pixels at the border of the  $5 \times 5$  event island. Two further filtering steps are then required to obtain the Level=2 event files, i.e. filter for bad grades (using ASCA grades) and for a “clean” status column and apply the Good Time Intervals (GTIs) supplied by the pipeline. The final step is to examine background light curves during each observation to detect and remove the periods of high background, due to flaring episodes. We perform the flare detection and removal following the recommendations suggested in Markevitch et al. (2003); both the total and the clean exposure times are listed in Table 1. Most of the observations are slightly affected by background flares thus we were able to use practically all the exposure time. The only exceptions are ObsID 3205, 4193, 906 and especially ObsID 1666, where  $\sim 29$  ks of the exposure were lost due to high background.

TABLE 1

OBSERVATION LOG FOR THE CHANDRA CLUSTER ARCHIVE SAMPLE. COLUMN (2) SHOWS THE REDSHIFT  $z$  OF THE CLUSTERS. THE COLUMNS (3), (4) AND (5) SHOW THE INSTRUMENT USED, THE OBSERVATION DATE AND THE OBSERVATION ID, RESPECTIVELY. THE COLUMNS (6) AND (7) SHOW THE OBSERVING TIME BEFORE ( $t_{exp}$ ) AND AFTER ( $t_{clean}$ ) THE REMOVAL OF HIGH BACKGROUND INTERVALS. COLUMN (9) IS THE GALACTIC COLUMN DENSITY  $N_H$  IN THE LINE OF SIGHT OF THE OBSERVATION.

Name	$z$	Instrument	Obs. Date	Obs. ID	$t_{exp}$ (ksec)	$t_{clean}$ (ksec)	$N_H$ ( $10^{20} \text{ cm}^{-2}$ )
A2034	0.113	ACIS-I	2001 May 05	2204	53.9	53.9	1.6
A1413	0.143	ACIS-I	2001 May 16	1661	9.7	9.7	2.2
		ACIS-I	2004 Mar 06	5003	76.1	75.0	
		ACIS-I	2005 Feb 03	5002	37.2	36.5	
A907	0.153	ACIS-I	2000 Jun 29	535	11.0	10.9	5.4
		ACIS-I	2002 Jun 14	3185	48.7	47.9	
		ACIS-I	2002 Oct 30	3205	47.7	40.5	
A2104	0.155	ACIS-S	2000 May 25	895	49.8	48.9	8.7
A1914	0.171	ACIS-I	2003 Sep 03	3593	18.9	18.8	0.9
A2218	0.176	ACIS-I	2001 Aug 30	1666	49.2	20.2	3.2
A963	0.206	ACIS-S	2000 Oct 11	903	36.8	35.8	1.4
A2261	0.224	ACIS-I	2004 Jan 14	5007	24.6	24.3	3.3
A2390	0.228	ACIS-S	2000 Oct 08	500	9.8	9.8	6.8
		ACIS-S	2003 Sep 11	4193	96.3	91.0	
A1835	0.253	ACIS-S	2000 Apr 29	496	10.8	10.3	2.3
ZwCl3146	0.291	ACIS-I	2000 May 10	909	46.6	45.6	3.0
A1995	0.319	ACIS-S	2000 May 08	906	57.5	53.8	1.4

### 2.1. Background Subtraction

An accurate subtraction of the background is crucial to perform a correct study of the spectral properties of the clusters in our sample, especially in their outskirts. Since we are dealing with extended objects, occupying most of the ACIS field of view we need to use a compilation of the blank-field observations, processed identically to the cluster observation (i.e. as described above) and reprojected onto the sky using the aspect information from the cluster pointing. It is worth noticing that the synthetic backgrounds correspond to longer exposure times ( $\sim 0.5$  Msec) than any of our observations, giving us a very good sampling in the estimate of the background to subtract. Moreover, in order to ‘tailor’ the background to our data we follow the recommendations given in the CIAO web-pages<sup>4</sup>. In particular we renormalize the blank-fields to the background in each observation, considering a region of the ACIS field of view practically free from cluster emission (mainly ACIS-S1 for ACIS-S observations, and ACIS-S2 for ACIS-I observations) and a spectral band (9.5-12 keV) where the Chandra effective area is nearly zero, therefore all the observed flux is due to the particle background.

In addition to the particle-induced background we check also if the diffuse soft X-ray background could be an important factor in our observations and if appropriate adjustments are needed. For each observation, we follow the procedure of Vikhlinin et al. (2005), extracting a spectra in the source-free regions of the detector, subtracting the renormalized blank-field background and fitting the residuals in XSPEC v11.3.2p (in the 0.4-1 keV band) with an unabsorbed *mekal* model, whose normalization was allowed to be negative. The best-fit model obtained is therefore included as an additional component in the spectral fits (with its normalization scaled by the area). However, in every observation the adjustments

required are minimal and do not affect significantly the determination of  $kT$  and  $Z$ , even at large radii. This is also due to the properties of the clusters in our sample, whose high  $kT$  values ( $> 4$  keV) even in the resolved outer regions are not affected significantly from the method applied for the subtraction of the diffuse soft background.

### 2.2. Cash statistics vs. $\chi^2$ statistics

The  $\chi^2$  statistics require grouping of the spectra, having at least 20 counts per bin, in order to be able to approximate the Poissonian distribution of counts with a Gaussian. On the contrary, Cash statistics do not require any grouping and represent a more reliable (and less biased) approach to fit the data. Indeed, it is well known from the literature (see e.g. Nousek & Shue 1989; Balestra et al. 2007) that the  $\chi^2$  statistics systematically ‘sees’ the observed spectra softer than the real ones. This usually leads to an overestimate of the slope of the observed spectra in the case of a simple power-law fit, while in the case that a thermal model is fitted to the data, the temperature measured is usually underestimated. As a test to see whether this systematics is present also in our data, we have decided to apply both these fit statistics. We find that for all the clusters of the sample, a systematically lower temperature is measured with the  $\chi^2$  (on average 7%–17% lower, depending on the cluster). On the other hand no obvious systematic trend is observed in the determination of  $Z$ , being the variation in the best-fitting value of the metallicity in each cluster ranging between  $\Delta Z \sim 0.01$  and  $\sim 0.07$  with no preferential direction. To avoid the dependence on the grouping method, and the bias in the best-fit temperature, we decide to use the modified Cash statistics, as implemented in XSPEC v11.3.2p, to determine the best-fit parameters and their uncertainties.

<sup>4</sup> [http://cxc.harvard.edu/cal/ACIS/Cal\\_prods/bkgnd/acisbg/COOKBOOK](http://cxc.harvard.edu/cal/ACIS/Cal_prods/bkgnd/acisbg/COOKBOOK)

### 2.3. Spectral Analysis

In order to study the radial properties of the cluster emission, we subdivide each cluster in annuli (circular or elliptical, depending on the morphology of the cluster) centered on the X-ray emission peak. In the more disturbed clusters, where an emission peak is not clearly identifiable, we assume the center of the cluster to correspond with the X-ray centroid at  $0.5r_{500}$ . We require each region to have at least  $\sim 7,000$  net counts, so that it would be possible to estimate the temperature and the metallicity of the annulus with sufficient accuracy. For each cluster the outermost annulus corresponds to an area where the intensity of the source in the 0.8-8 keV band is roughly equal to that of the background. We extract a spectra from each annulus after excluding the  $3\sigma$  point sources detected by the CIAO tool *wavdetect*. The source list produced is also inspected 'by-eye' in order to remove possible additional sources not detected by *wavdetect* (especially in the regions where the diffuse emission from the cluster is brighter). The CIAO script used to perform the spectral extraction is *specextract*, which generates source and background spectra and build the appropriate RMFs and ARFs. The background is taken from the re-normalized blank field observations using the same region of the source.

The spectra are analyzed with XSPEC v11.3.2p (Arnaud et al. 1996) and fitted by a single-temperature *mekal* model (Kaastra 1992; Liedahl et al. 1995) in which the ratio between the elements is fixed to the solar value as in AG89. However, as explained in §1, these values for the solar metallicities have more recently been superseded by the new values by Grevesse & Sauval (1998) and A05. For clarity and completeness, we also performed the fits using solar abundances by A05. The free parameters in the model are the temperature  $kT$ , the metallicity  $Z$  of the gas and the normalization. The spectral band considered in the fit is the 0.6-8 keV. We choose not to consider the data below 0.6 keV because of uncertainties in the ACIS calibration below that energy. The  $N_H$  derived from the X-rays is found to be consistent (within  $1\sigma$ ) with the Galactic value in the line of sight of each observation, as derived from radio data (Stark et al. 1992), except in the cases of A2104 and A2390 (see Table 1 and following § 2.4). In these clusters the  $N_H$  value measured from X-ray data is significantly different (at more than  $2\sigma$  confidence level) from the radio value, therefore we adopt the X-ray value. The  $N_H$  value is fixed to the Galactic value obtained from the radio data (and listed in Table 1) in the rest of the sample. We have measured  $N_H$  from the X-ray data in each annulus, finding no evidence of radial variation. Therefore,  $N_H$  is fixed to the same value in all the radial annuli.

We have divided then our sample in Cooling-Core and Non-Cooling-Core clusters according to their central cooling time. The gas temperature and density profiles are recovered from the single-phase spectral fit done in annular rings by correcting the emissivity in each shell by the contribution of the outer shells moving inwards. A detailed description of the procedure is presented in Ettori et al. (2002). In brief, the normalization of the thermal component, being proportional to the Emission Integral, provides the gas density, whereas the deprojected temperature is provided by weighting for the corrected emissivity the spectral measurement. The deprojected values in the innermost bin are then used to estimate

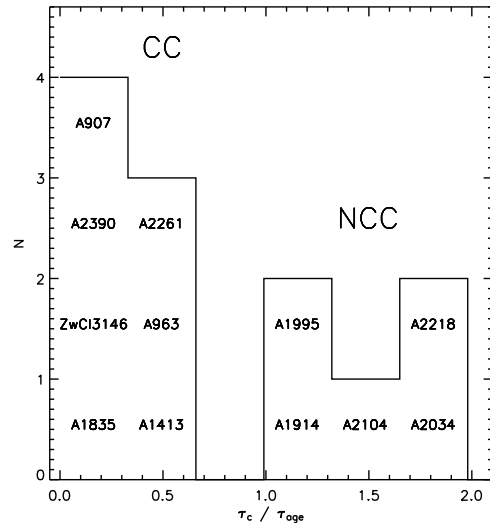


FIG. 1.— Histograms of the distribution in our sample of the values of  $\tau_c/\tau_{age}$ , computed as described in § 3 and quoted in Table 2.

the central cooling times  $\tau_c = 5/2(\mu_e/\mu)T_e(n_e/\epsilon)$ , where  $\mu = 0.613$  and  $\mu_e = 1.174$  are appropriate for a plasma with a metallicity of 0.3 times the solar values in AG89,  $T_e$ ,  $n_e$  and  $\epsilon$  are the gas temperature, electron density and emissivity in the innermost bin, respectively.

The central cooling times are reported in Table 2, as well as the age  $\tau_{age}$  of each cluster, and the ratio between the two quantities. The age of the Universe at the  $z$  of observation is used as an upper limit to the age of the cluster. Bauer et al. (2005) computed the cooling times for 6 of the clusters in our sample (A1835, A1914, A2218, A2261, A2390 and ZwCl3146) finding a  $\tau_c$  in the center of the cluster, or at 50 kpc, consistent with the values computed for the central bin in our spectral analysis (which might extend farther out than 50 kpc from the center in some cases). Following their criterium, a clear separation between the CC and the NCC in our sample can be located at  $\tau_c \sim 10$  Gyr (Figure 1; corresponding to  $\tau_c/\tau_{age} \sim 1$ ). We have 4 clusters presenting signs of strong cooling ( $\tau_c < 2$  Gyr) and 3 clusters exhibiting signs of mild cooling ( $\tau_c < 10$  Gyr). The remaining 5 clusters can be classified as NCC, presenting longer cooling times in the center. The projected temperature and metal abundance profiles for both CC and NCC objects are shown in Figures 2 and 3.

#### 2.4. Notes on individual clusters

**A2034:** A2034 ( $z=0.113$ ) has been observed with Chandra in one ACIS-I pointing (ObsID: 2204). The temperature profile we derived is quite flat in the central regions of the cluster, where the temperature is  $kT \sim 8$  keV. It shows however a negative gradient after 400 kpc from the center. A similar trend is observed in the metallicity, where the average value of  $Z = 0.4$  within 400 kpc from the center decreases to  $Z < 0.2$  at larger radii.

**A1413:** A1413 ( $z=0.143$ ) has been observed four times with ACIS-I. We discard one observation (ObsID: 537) which is affected almost entirely by a persisting flare. In one of the observations used in our analysis (ObsID:

TABLE 2

GLOBAL CLUSTER PROPERTIES OF THE CHANDRA SAMPLE. COLUMN (2) SHOWS THE TOTAL NET COUNTS FROM THE INNER TO THE OUTER ANNULUS CONSIDERED IN THE SPECTRAL ANALYSIS. THE COLUMNS (3), (4) AND (5) SHOW THE GLOBAL TEMPERATURE  $\langle kT \rangle$ , THE GLOBAL METALLICITY  $\langle Z \rangle$  AND THE VIRIAL RADIUS  $r_{180}$ , COMPUTED WITHIN  $0.07 - 0.4r_{180}$ , RESPECTIVELY. COLUMN (6) SHOWS THE APERTURE USED TO MEASURE  $\langle kT \rangle$  AND  $\langle Z \rangle$ . THE COLUMNS (7) AND (8) SHOW THE CENTRAL COOLING TIMES AND THE RATIO WITH RESPECT TO THE AGE OF THE UNIVERSE AT THE CLUSTER REDSHIFT.

Name	Net cts (0.6-8 keV)	$\langle kT \rangle$ (keV)	$\langle Z \rangle$ ( $Z_{\odot}$ )	$r_{180}$ (kpc)	Aperture ( $''$ )	$\tau_c$ (Gyr)	$\tau_c/\tau_{age}$
A2034	78,900	$6.36 \pm 0.15$	$0.30 \pm 0.04$	2,222	76-433	$21.2 \pm 3.2$	$1.77 \pm 0.27$
A1413	181,500	$7.52^{+0.20}_{-0.12}$	$0.23 \pm 0.03$	2,416	67-385	$4.2 \pm 0.3$	$0.36 \pm 0.03$
A907	87,500	$5.82 \pm 0.12$	$0.34 \pm 0.04$	2,125	56-320	$2.0 \pm 0.1$	$0.17 \pm 0.01$
A2104	63,100	$6.76 \pm 0.19$	$0.24 \pm 0.05$	2,290	60-341	$18.1 \pm 2.1$	$1.58 \pm 0.18$
A1914	39,100	$9.20^{+0.39}_{-0.37}$	$0.27 \pm 0.07$	2,672	64-367	$12.2 \pm 1.0$	$1.07 \pm 0.09$
A2218	18,300	$6.25 \pm 0.31$	$0.24 \pm 0.07$	2,202	52-295	$21.3 \pm 1.8$	$1.89 \pm 0.16$
A963	41,800	$6.02^{+0.28}_{-0.19}$	$0.18 \pm 0.06$	2,161	45-256	$6.5 \pm 0.4$	$0.59 \pm 0.04$
A2261	21,500	$7.43^{+0.49}_{-0.27}$	$0.30^{+0.07}_{-0.06}$	2,400	47-267	$7.0 \pm 0.4$	$0.65 \pm 0.03$
A2390	202,600	$9.35 \pm 0.15$	$0.30 \pm 0.03$	2,693	52-295	$1.3 \pm 0.2$	$0.12 \pm 0.02$
A1835	23,100	$8.06 \pm 0.53$	$0.31 \pm 0.09$	2,500	44-254	$0.9 \pm 0.1$	$0.08 \pm 0.01$
ZwCl3146	40,500	$8.59 \pm 0.39$	$0.24 \pm 0.06$	2,582	41-237	$1.0 \pm 0.1$	$0.10 \pm 0.01$
A1995	30,200	$7.59^{+0.57}_{-0.44}$	$0.50^{+0.12}_{-0.11}$	2,427	37-209	$12.7 \pm 1.3$	$1.28 \pm 0.14$

5003) the source is placed in a position of the ACIS-I array very close to the S2 chip, therefore S2 is still contaminated by source emission and we can not use it to re-normalize the blank field to the background in the observation. We use instead part of the I1 chip (which is front-illuminated as S2) to re-normalize, since it is more distant from the cluster center than S2 and therefore less contaminated by cluster emission. The resulting temperature profile shows a slight decrease in temperature towards the center ( $\Delta kT = 1.2^{+0.7}_{-0.6}$  keV within the inner 150 kpc). A1413 has been also observed by XMM-Newton (Pratt & Arnaud 2002), representing one of the clusters with the most accurate temperature profile observed by this satellite. This cluster is also part of the sample of Chandra clusters analyzed by Vikhlinin et al. (2005). The XMM-Newton observation does not find any evidence of a cool core, in contrast with the temperature profiles obtained with Chandra both in our analysis and even more evidently in Vikhlinin et al. (2005). This might be due to the poorer angular resolution of XMM-Newton with respect to Chandra.

The metallicity profile is decreasing towards larger radii, and consistent within  $1\sigma$  with the measures of Vikhlinin et al. (2005).

**A907:** A907 ( $z=0.153$ ) has been observed with Chandra in three separate ACIS-I pointings (ObsID: 535, 3185 and 3205), all of them used in our analysis. The temperature profile shows an evidence of a cool core in the center of the cluster ( $\Delta kT = 1.4^{+0.2}_{-0.3}$  keV in the central 100 kpc). The metallicity profile presents a decreasing trend toward larger radii. A907 is also part of the cluster sample analyzed by Vikhlinin et al. (2005). Their results, both for the temperature and the metallicity, are fully consistent with ours within the  $1\sigma$  statistical uncertainties.

**A2104:** A2104 ( $z=0.155$ ) has been observed with Chandra in one ACIS-S pointing (ObsID: 895). As described in § 2.3, the value of the  $N_H$  measured from the X-ray data alone is significantly different from the radio value, thus we have decided to fix the  $N_H$  to the best fit value obtained from the fit ( $1.55 \times 10^{21} \text{ cm}^{-2}$ ). The

cluster does not show any evidence of a cool core in its center, having a temperature profile decreasing towards the outskirts. The metallicity profile is consistent with being flat, with a value  $Z \sim 0.3 - 0.4Z_{\odot}$ , within the  $1\sigma$  uncertainties.

**A1914:** Two ACIS-I pointings of A1914 ( $z=0.171$ ) are available in Chandra archive. However the oldest (and shortest) observation (ObsID: 542) has been performed in 1999. For observations performed in that year an accurate modeling of the ACIS background is not currently available. Thus to avoid problems in background subtraction we have decided to discard it and keep only the longest observation (ObsID: 3593). A negative gradient in  $kT$  is quite clear: the temperature drops from  $kT = 12.0^{+0.9}_{-0.6}$  keV in the center down to  $kT = 8.5 \pm 0.6$  keV in the outer radial bin. A similar trend is observed also in the abundance profile, where  $Z = 0.5 \pm 0.1Z_{\odot}$  in the center, then decreasing to  $0.2 \pm 0.1Z_{\odot}$  in the two outer radial bins. This is one of the few examples of metallicity peak without a corresponding cool core (or temperature drop) towards the center.

**A2218:** A2218 ( $z=0.176$ ) has been observed three times with ACIS-S. Unfortunately two of these observations (ObsID: 553 and 1454) were performed in 1999 and for the reason described in the case of A1914 we have decided to discard them. Moreover the remaining observation (ObsID: 1666) has been strongly affected by a flare which reduces the good exposure time to only  $\sim 20$  ks. With these data we are able to observe the presence of a centrally peaked temperature profile (a hot, instead of a cool core) and a constant metallicity profile. A temperature profile peaked toward the center has been also seen by Machacek et al. (2002), analyzing the two Chandra observations performed in 1999. This is consistent with the picture of A2218 being involved in a line-of-sight merger, as suggested by a considerable disturbance of the intracluster gas in the X-rays and by the observed substructure in the optical (e.g. Pratt et al. 2005).

**A963:** A963 ( $z=0.206$ ) has been observed with Chandra in one ACIS-S pointing (ObsID: 903). We found a decreasing trend of  $Z$  with the radius, with only a very

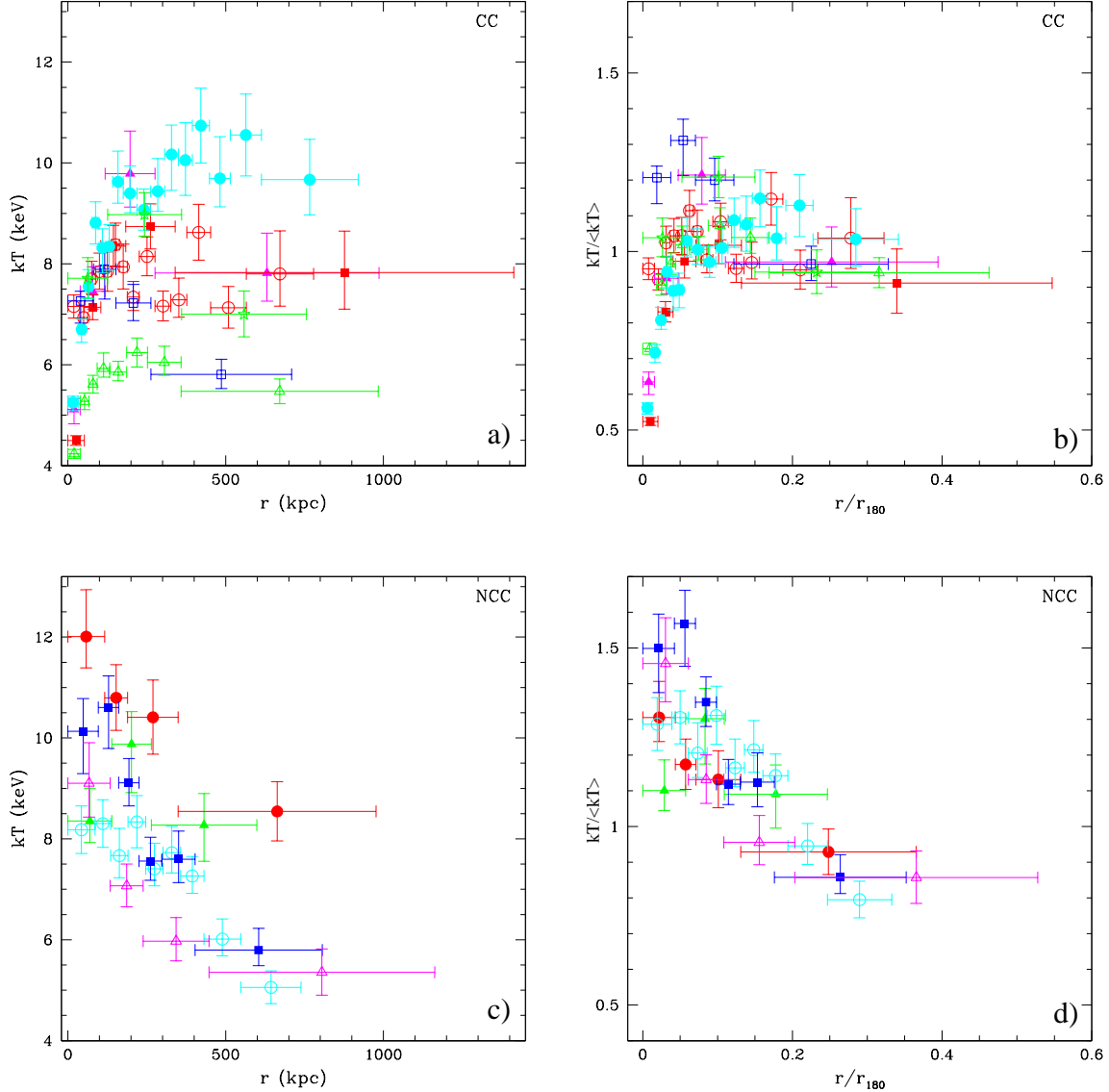


FIG. 2.— *a)*: Temperature profiles for the CC clusters in the sample: A907 (green empty triangles), A963 (blue empty squares), A1413 (red empty circles), A1835 (magenta filled triangles), A2261 (green stars), A2390 (cyan filled circles) and ZwCl3146 (red filled squares). *b)*: Normalized temperature profiles for the CC clusters, plotted against the radii in units of  $r_{180}$ . The symbols have the same meaning as in panel *a)*. *c)*: Temperature profiles for the NCC clusters in the sample: A1914 (red filled circles), A1995 (green filled triangles), A2034 (cyan empty circles), A2104 (blue filled squares) and A2218 (magenta empty triangles). *d)*: Normalized temperature profiles for the NCC clusters, plotted against the radii in units of  $r_{180}$ . The symbols have the same meaning as in panel *c)*.

weak hint for the presence of a lower temperature in the center.

**A2261:** Two pointings of A2261 ( $z=0.224$ ) are available in the Chandra archive. One of the observations (ObsID: 550) has been performed in 1999 and therefore we discard it for the reason described above in the case of A1914. The temperature profile does show only a hint (more than  $2\sigma$  however) of a decrease in the center, where the temperature drops down from  $9.0 \pm 0.4$  keV to  $7.7 \pm 0.4$  keV. The metallicity profile shows a constant behaviour for the first two bins and a decrease (significant at more than  $1\sigma$ ) in the outer radial bin.

**A2390:** A2390 ( $z=0.228$ ) has been observed three times with ACIS-S. One of the observations (ObsID: 501) has been performed in 1999 and therefore we discard it.

We concentrate our analysis on the remaining two observations (ObsID: 500 and 4193), yielding a total of  $\sim 100$  ks of good observing time. The value of the  $N_H$  derived from the X-rays ( $N_H = 1.1 \times 10^{21} \text{ cm}^{-2}$ ) is significantly different than the radio value, therefore we adopted the X-ray value in the spectral fits. A2390 is also part of the sample analyzed in Vikhlinin et al. (2005). Similarly to them we find a cool core ( $kT = 5.8 \pm 0.2$  keV) in the center of the cluster with a  $kT$  profile getting flatter going towards the outskirts, being fully consistent with their measured temperatures at every radius. On the other hand, the metallicity profile shows just a hint of a peak in the central part of the cluster. It is however consistent at  $1\sigma$  with the profile of Vikhlinin et al. (2005) and not sensitive to the choice of the  $N_H$ .

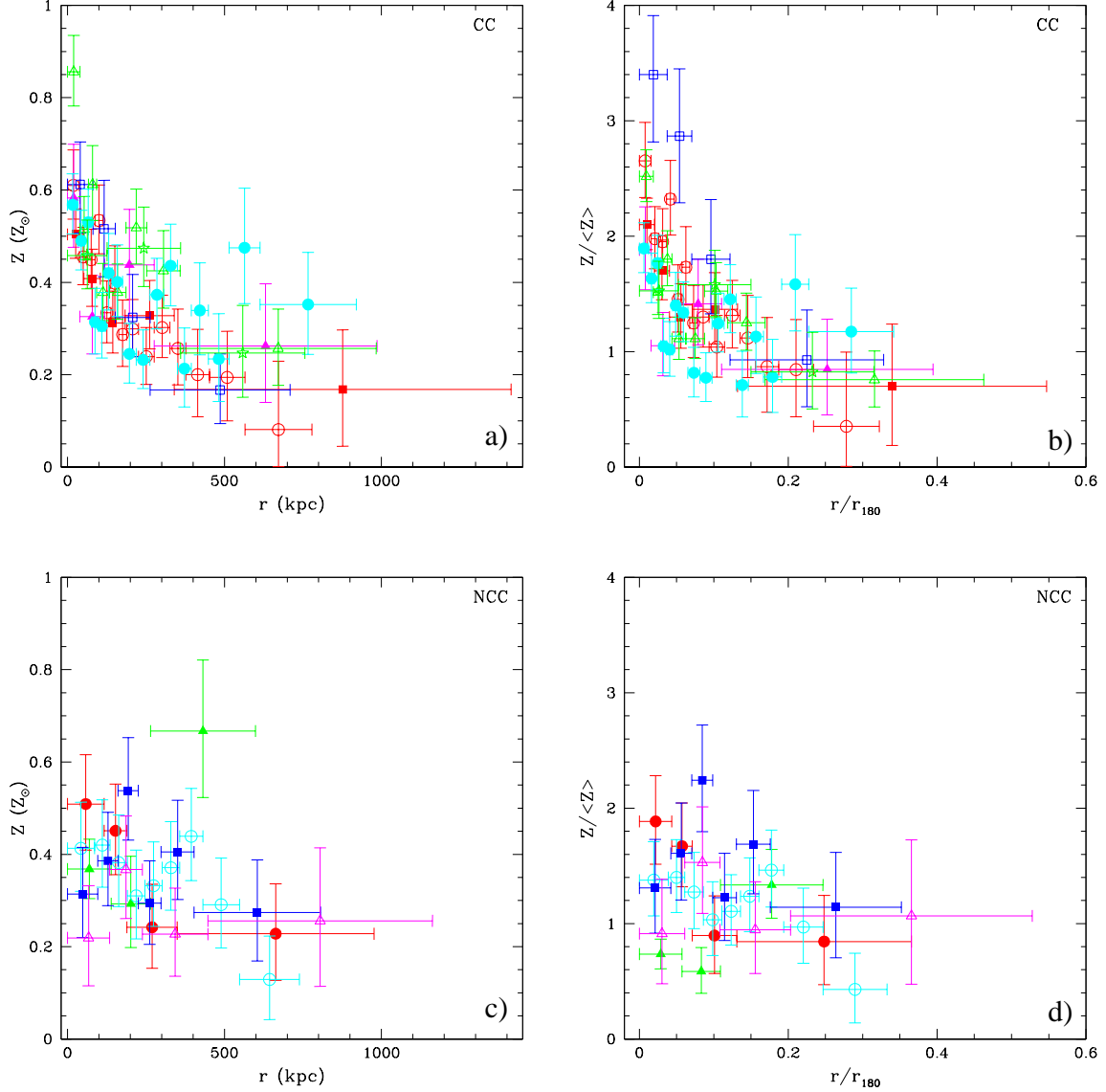


FIG. 3.— *a)*: Abundance profiles for the CC clusters in the sample: the different symbols correspond to the clusters listed in Figure 2a. *b)*: Normalized abundance profiles for the CC clusters, plotted against the radii in units of  $r_{180}$ . The symbols have the same meaning as in panel a). *c)*: Abundance profiles for the NCC clusters in the sample: the different symbols correspond to the clusters listed in Figure 2c. *d)*: Normalized abundance profiles for the NCC clusters, plotted against the radii in units of  $r_{180}$ . The symbols have the same meaning as in panel c)

**A1835:** Two different ACIS-S observations of A1835 ( $z=0.253$ ) are present in the Chandra archive. We discard the older (and longer) observation (ObsID: 495), performed in 1999 because of the reason described in the case of A1914, keeping only the  $\sim 10$  ks observation performed in 2000 (ObsID: 496). The temperature profile of A1835 shows a clear evidence of a cool core in its center where  $kT$  drops down by a factor of  $\sim 2$ . Moreover the temperature shows a decline after 300 kpc, going toward larger radii. Piffaretti et al. (2005) analysed XMM-Newton observations of A1835 and detected a temperature decrease at large radii, as in our data. Majerowicz et al. (2002) also analysed XMM-Newton data and found a decrease in the temperature profile at large radii (at  $\sim 400$  kpc from the center); however their temperature profile becomes constant after such decrease. The de-

crease at large radii has not been observed in the analysis of Chandra data by Voigt & Fabian (2006), who found a constant temperature outside the central 100 kpc. However it is worth noticing that in their work they analysed the 1999 observation (instead of the 2000 observation, as in our analysis) which might have background subtraction problems especially at large radii. This may explain the difference between the two profiles. The metallicity profile shows a decreasing gradient in the first two bins, becoming constant afterwards. The only comparison with the literature comes from an XMM-Newton observation analyzed by Majerowicz et al. (2002), where an almost constant metallicity profile at every radius has been observed.

**ZwCl13146:** ZwCl13146 ( $z=0.291$ ) has been observed with ACIS-I in one pointing (ObsID: 909). Also this

cluster clearly shows the presence of a cool core ( $kT$  dropping down by a factor of almost 2). A decreasing trend in metallicity from  $Z = 0.50 \pm 0.05$  in the center, down to  $Z = 0.17 \pm 0.12$  in the outer bin, is also observed.

**A1995:** One ACIS-S observation of A1995, the farthest cluster in our sample ( $z=0.319$ ), is present in the Chandra archive (ObsID: 906). Although this observation is quite long ( $\sim 50$  ks of good exposure time) the number of counts available allowed us to divide this cluster only in three radial bins. The temperature profile of A1995 is consistent to be flat within the errors with a temperature around 9 keV. The abundance profile seems to have a positive gradient in the outer bin, however the errors are large and this increase in  $Z$  is not very significant.

### 3. SELF-SIMILARITY OF RADIAL PROFILES

One of the main goals of this paper is to look for a (purely phenomenological) self-similarity in the radial profiles of temperature and metallicity, after they are scaled to the cluster virial radius  $r_{180}$ . A measure of  $r_{180}$  is thus crucial to test for such self-similarity in our cluster sample. This quantity can be approximated by the following relation:

$$r_{180} = 1.95h^{-1} \text{ Mpc}(\langle kT \rangle / 10 \text{ keV})^{1/2}, \quad (1)$$

as calibrated from the non-radiative hydrodynamical simulations of clusters by Evrard et al. (1996). It is worth noticing that this relation is in agreement with the scaling relations observed (e.g. Ettori et al. 2004) in the X-rays, where the dependency on  $kT$  is consistent with Eq.(1) and only the absolute normalization may experience some variations. To compute the global temperature  $\langle kT \rangle$  necessary to estimate  $r_{180}$  we extract spectra including emission going from  $0.07r_{180}$  to  $0.4r_{180}$  in each cluster. The central regions of each cluster are therefore excluded from the spectra in order to avoid contamination from a possible cool core. The values of  $\langle kT \rangle$  and  $r_{180}$  have been evaluated iteratively until a convergence to a stable value of the temperature is obtained ( $\Delta kT \leq 0.01$  keV between two different iterations). From the fits we are able to determine also a global metallicity  $\langle Z \rangle$  in each cluster. In Table 2 we list the best-fit values for  $\langle kT \rangle$  and  $\langle Z \rangle$ , and the value of  $r_{180}$  computed using the formula above. The minimum and maximum apertures used to extract the total spectrum are listed as well.

#### 3.1. The temperature profiles

Figure 2 shows the normalized temperature profiles for all the CC clusters (panel b) compared with the NCC clusters (panel d). This figure has been obtained by normalizing the temperatures in each cluster to its average temperature  $\langle kT \rangle$  computed from the total cluster spectrum excluding the central  $0.07r_{180}$ . The error-weighted mean and the best-fit results after fitting with single power-laws  $Y \propto r^\mu$  are presented in Table 3.

Within  $0.1r_{180}$ , the temperature profiles in CC objects increases with a slope  $\mu = 0.25$ . Moving outwards, between  $0.1r_{180}$  and the outer radial limit of our spectral analysis at  $\approx 0.5r_{180}$ , these profiles behave as  $r^{-0.1}$ . Non-cooling-cores systems have, on average, a profile that is almost flat at  $r < 0.1r_{180}$  and then decreases rapidly as

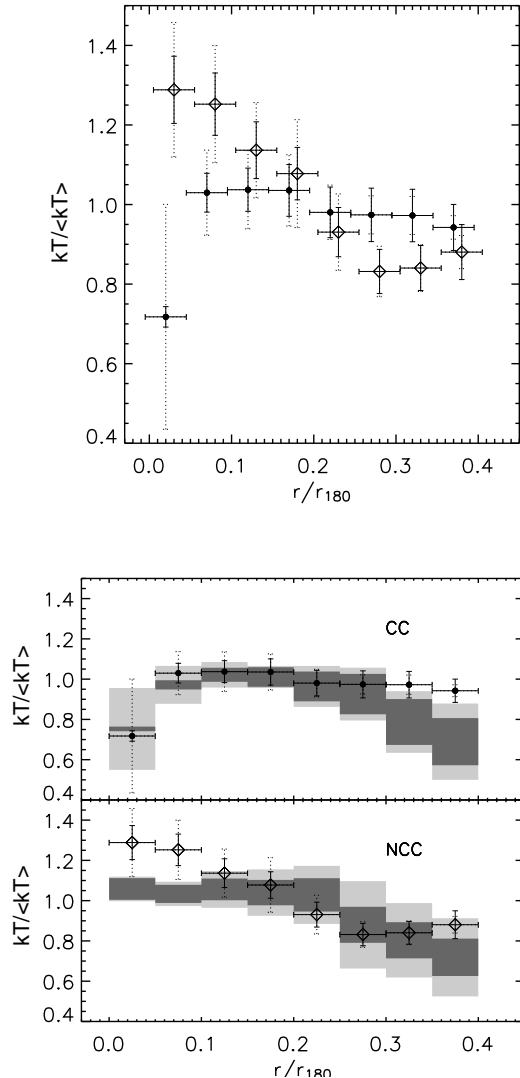


FIG. 4.— Error-weighted mean temperature profile of the CC (filled circles) and NCC (open diamonds) clusters in our sample at intermediate redshift (top panel). (Bottom) Comparison between our results and the local measurements in DM02 (shaded regions). The  $1\sigma$  errors on the means are plotted as solid lines (dark gray region for the local estimates) while the scatter (rms) in each data bin is shown as a dotted line (light gray region for local estimates).

$r^{-0.3}$ . In the outskirts, the temperature profiles of CC and NCC clusters show a significant discrepancy between their slopes, being NCC more deviant from the isothermal case.

Our best fit functional for the CC sample is fully consistent with the best fit functional form found by Vikhlinin et al. (2005) in their sample of CC clusters, at  $r \lesssim 0.3r_{180}$ . The two functionals diverge significantly only above  $0.3r_{180}$ , where our profile is flatter (and therefore the value of  $kT/\langle kT \rangle$  is higher) than Vikhlinin et al. (2005) profile. However, only a few of our data points are located beyond that radius, preventing us from any statistically significant comparison between the two samples at  $r \gtrsim 0.3r_{180}$ .

Adopting the A05 abundances has not changed the best-fit values of  $kT$  at every radius (always fully consistent within the  $1\sigma$  errors) in the individual clusters,



TABLE 3

ERROR-WEIGHTED MEANS, WITH ERRORS ON THE MEAN AND R.M.S. QUOTED WITHIN ROUND BRACKETS, AND BEST-FIT PARAMETERS OF THE SINGLE POWER-LAWS  $Y = Y_{0.1}(x/0.1)^\mu$ , WITH  $x = r/r_{180}$ .  $\langle kT \rangle$  AND  $\langle Z \rangle$  ARE MEASURED IN THE RADIAL RANGE  $0.07 - 0.4r_{180}$ .

	$kT/\langle kT \rangle$		
	all $r$	$r < 0.1r_{180}$	$r > 0.1r_{180}$
All	$0.84 \pm 0.04(0.28)$ $Y_{0.1} = 1.00 \pm 0.01$ $\mu = 0.15 \pm 0.01$ $\chi^2/\text{dof}=1223.4/78$	$0.79 \pm 0.03(0.35)$ $Y_{0.1} = 1.20 \pm 0.01$ $\mu = 0.26 \pm 0.01$ $\chi^2/\text{dof}=720.0/43$	$1.02 \pm 0.06(0.10)$ $Y_{0.1} = 1.10 \pm 0.02$ $\mu = -0.16 \pm 0.03$ $\chi^2/\text{dof}=59.1/33$
CC	$0.80 \pm 0.04(0.24)$ $Y_{0.1} = 1.00 \pm 0.01$ $\mu = 0.17 \pm 0.01$ $\chi^2/\text{dof}=744.3/52$	$0.76 \pm 0.03(0.26)$ $Y_{0.1} = 1.16 \pm 0.02$ $\mu = 0.25 \pm 0.01$ $\chi^2/\text{dof}=496.3/30$	$1.02 \pm 0.06(0.08)$ $Y_{0.1} = 1.07 \pm 0.02$ $\mu = -0.10 \pm 0.03$ $\chi^2/\text{dof}=26.7/20$
NCC	$1.13 \pm 0.07(0.20)$ $Y_{0.1} = 1.12 \pm 0.01$ $\mu = -0.15 \pm 0.01$ $\chi^2/\text{dof}=76.6/24$	$1.27 \pm 0.08(0.14)$ $Y_{0.1} = 1.25 \pm 0.04$ $\mu = -0.02 \pm 0.03$ $\chi^2/\text{dof}=28.8/11$	$1.02 \pm 0.07(0.13)$ $Y_{0.1} = 1.23 \pm 0.04$ $\mu = -0.32 \pm 0.05$ $\chi^2/\text{dof}=17.1/11$
	$Z/\langle Z \rangle$		
	all $r$	$r < 0.1r_{180}$	$r > 0.1r_{180}$
All	$1.31 \pm 0.29(0.54)$ $Y_{0.1} = 1.13 \pm 0.04$ $\mu = -0.23 \pm 0.02$ $\chi^2/\text{dof}=149.2/78$	$1.41 \pm 0.26(0.60)$ $Y_{0.1} = 1.03 \pm 0.06$ $\mu = -0.28 \pm 0.03$ $\chi^2/\text{dof}=120.7/43$	$1.11 \pm 0.33(0.32)$ $Y_{0.1} = 1.35 \pm 0.10$ $\mu = -0.44 \pm 0.15$ $\chi^2/\text{dof}=20.0/33$
CC	$1.40 \pm 0.28(0.58)$ $Y_{0.1} = 1.17 \pm 0.05$ $\mu = -0.24 \pm 0.03$ $\chi^2/\text{dof}=80.2/52$	$1.53 \pm 0.26(0.62)$ $Y_{0.1} = 1.11 \pm 0.06$ $\mu = -0.27 \pm 0.03$ $\chi^2/\text{dof}=64.9/30$	$1.12 \pm 0.32(0.33)$ $Y_{0.1} = 1.37 \pm 0.11$ $\mu = -0.52 \pm 0.18$ $\chi^2/\text{dof}=11.0/20$
NCC	$1.06 \pm 0.31(0.44)$ $Y_{0.1} = 1.06 \pm 0.07$ $\mu = 0.00 \pm 0.07$ $\chi^2/\text{dof}=41.7/24$	$1.05 \pm 0.28(0.56)$ $Y_{0.1} = 1.08 \pm 0.15$ $\mu = 0.03 \pm 0.14$ $\chi^2/\text{dof}=31.7/11$	$1.08 \pm 0.36(0.31)$ $Y_{0.1} = 1.27 \pm 0.20$ $\mu = -0.29 \pm 0.27$ $\chi^2/\text{dof}=8.5/11$

therefore the best fit functionals representing both the CC and the NCC sample have not varied.

A clearer picture can be seen also if we compute an error-weighted average of the  $kT$  profiles in several bins of width 0.05 in  $r/r_{180}$ . The contribution to the single bin is provided from the measurements (and relative error) that fall into that bin, weighted in proportion to the percentage of the spatial coverage of the bin. The error-weighted mean  $kT/\langle kT \rangle$  profile is plotted in Figure 4 and compared with the local estimates from DM02. CC and NCC objects show well defined opposite gradient in the inner radial and more similar behaviour moving outwards. A good agreement is also observed with the local profiles, apart from two significant deviations: (i) our CC mean profile appears flatter at  $r > 0.2r_{180}$ , with an error-weighted value of  $0.97 \pm 0.06$  (r.m.s. 0.07), to be compared with the local value of  $0.85 \pm 0.11$  (r.m.s. 0.16), (ii) our NCC profile is steeper within  $0.1r_{180}$ , with a mean value of  $1.27 \pm 0.08$  (r.m.s. 0.14) with respect to the local value of  $1.04 \pm 0.05$  (r.m.s. 0.07).

### 3.2. The metal abundance profiles

The metallicity profiles are plotted against the radius normalized to  $r_{180}$  for the CC and NCC sample in Figure 3b and 3d, respectively. A different behaviour in the very central regions between the two samples is quite clear. To characterize this behaviour, we have fitted the normalized profiles  $Z/\langle Z \rangle$  with respect to  $r/r_{180}$  with single power-laws  $Y \propto r^\mu$  over different radial ranges. While

the NCC clusters presents a flat profile within  $\sim 0.1r_{180}$ , a sharper negative gradient is observed in the CC cluster sample ( $\mu = -0.24$ ; see Table 3). Also at  $r > 0.1r_{180}$ , where a model with a single power-law well reproduce the data (reduced  $\chi^2$  less than 1), the CC clusters show hints of a steeper profile ( $\mu = -0.52 \pm 0.18$  in the CC sample,  $\mu = -0.29 \pm 0.27$  in the NCC sample).

We compute an error-weighted average  $Z$  profile as done for the temperature profile and compare it with the local measurements in DM01, after scaling the radii to  $r_{180}$  (see Figure 5). The two profiles are in agreement at  $r > 0.1r_{180}$ , with both subsamples showing an evidence for a negative gradient in metallicity significant at least at  $2\sigma$ . A different behaviour between the two subsample is observable in the central bin, where the value in the CC sample is  $\sim 20\% - 30\%$  higher than in the NCC sample. It is worth noticing that all the clusters in our sample have  $kT > 6$  keV and this trend may be different in lower temperature clusters. DM01 in their analysis observed a clear gradient in the metallicity profiles of their CC clusters, while the profiles of their NCC clusters were almost constant. Moreover the average metallicity observed in the CC clusters was systematically higher than in the NCC sample, at least within  $\sim 0.3r/r_{180}$  from the center. In our analysis, we do not find a clear difference between the CC and NCC abundance profiles as in DM01. Except for the inner radial bin where the metallicity in CC objects can be higher by 50 per cent

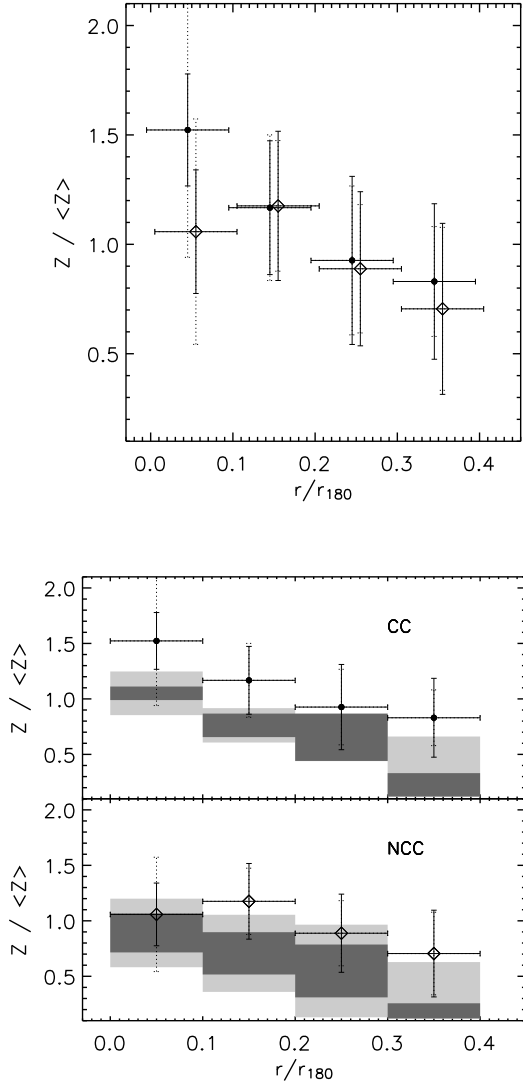


FIG. 5.— Error-weighted mean metal abundance profile of the CC (filled circles) and NCC (open diamonds) clusters in our sample at intermediate redshift (top panel). (Bottom) Comparison between our results and the local measurements in DM01 (shaded regions). The  $1\sigma$  errors on the means are plotted as solid lines (dark gray region for the local estimates) while the scatter (rms) in each data bin is shown as a dotted line (light gray region for local estimates).

than in NCC ones, the CC and NCC profiles are very similar and consistent within the errors.

To compare our mean values at intermediate redshift with the results obtained locally from DM01, we estimate an error-weighted average  $Z$  profile for both CC and NCC objects in local and intermediate  $z$  samples (Figure 5). While the slope of the profiles is generally in agreement with DM01 for the both the CC and NCC clusters, the value of  $Z/\langle Z \rangle$  is systematically higher in our sample with respect to the DM01 sample, with differences up to 50% within  $0.1r_{180}$  of CC systems. This might be due to the different method used to compute  $\langle Z \rangle$ , being in DM01 work estimated as fit with a constant to the radial metallicity profile. However, apart from the inner radial region, the discrepancy between the local profiles and the ones at intermediate redshifts

are within  $1\sigma$ . Using the same method to determine  $\langle Z \rangle$  on our data, we find that the values of  $Z/\langle Z \rangle$  are fully consistent with DM01.

### 3.3. Comparison with the new compilations of solar values

All the analysis described in the current section has been performed adopting the AG89 compilation of photospheric abundances. This choice has been due mainly by the necessity to have a direct comparison with previous works in the literature (e.g. DM01). However, as explained above in §1, the abundance values listed in AG89 have been recently superseded by the new photospheric values by Grevesse & Sauval (1998) and A05, who introduced a 0.676 and 0.60 times lower Iron solar abundance, respectively. Therefore, we have also performed the fits using solar abundances by A05 to check whether adopting the "old" AG89 values might have introduced any bias in our analysis.

The shape of the  $Z$  profile for both the CC sample and the NCC sample resembles very closely that observed in Figure 5 for the AG89 values of  $Z$ . However to better quantify this comparison we fitted also these new values with a power-law functional. We measure

$$Z_{CC}/\langle Z \rangle = 0.67 \pm 0.06 x^{-0.25 \pm 0.03}, \quad (2)$$

$$Z_{NCC}/\langle Z \rangle = 1.00^{+0.20}_{-0.18} x^{-0.02 \pm 0.07}, \quad (3)$$

with  $x \equiv r/r_{180}$ . If we compare the result of the fit with the last two rows in the first column in Table 3, it is quite clear that the slope of the power-law in both the CC and NCC sample is consistent with what we obtained using the AG89 values (well within the  $1\sigma$  uncertainties) and the difference is only in the normalization. As expected, this result might indicate that our metallicities are mostly driven by Iron and that the contribution of the  $\alpha$  elements to the determination of the abundances is negligible. Indeed, all our clusters have a temperature larger than  $\sim 6$  keV, therefore the abundance measures are dominated by the Fe-K $\alpha$  line. As a further test to this hypothesis we tried to fit the Fe abundance independently from the  $\alpha$  elements abundances. To this aim we used a *vmekal* model where the abundances of O, Mg, Si and S were tied-up to the same value and fitted as a single free parameter (in order to reduce the number of free parameters), while the other elements (apart from Fe) were frozen at solar. While the Fe abundance remained always consistent with the value of  $Z$  measured considering the metallicity as a single parameter, in almost all the spectra we could not find any statistically significant detection of a contribution from  $\alpha$  elements. Their abundances has been measured as upper limits in most cases (generally  $Z_\alpha < 0.3$ ), and as very low values in the rest of the spectra (generally  $Z_\alpha \sim 0.1 - 0.2$ , often consistent with  $Z_\alpha \sim 0$  at  $1\sigma$ ). This is true even in the inner part of the clusters in the sample, where the signal-to-noise of the spectra is higher and in principle it may be easier to detect the presence of elements other than Iron.

These results suggest that the measure of  $Z$  in our cluster sample consists mainly in a measure of Iron metallicity. Therefore, adopting the AG89 solar abundances instead of the A05 (which have different  $Z_{Fe}/Z_\alpha$  ratios) produces only a difference in the value of the relative  $Z$  measured. This does not introduce any bias in the analysis of the radial profiles, since the absolute value of  $Z$

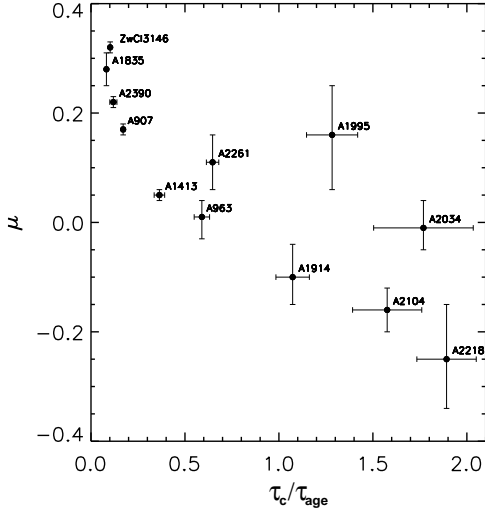


FIG. 6.— Distribution of the exponential  $\mu$  in the relation  $kT/\langle kT \rangle = A (r/r_{180})^\mu$  as a function of  $\tau_c/\tau_{age}$ .

does not change and only the reference value assumed for the solar metallicity experience a variation.

### 3.4. Gradients and cooling times

We investigate the correlation of the central slopes of the temperature and metallicity profiles with the central cooling time in each cluster. To this aim, the values of  $kT(r)/\langle kT \rangle$ ,  $Z(r)/\langle Z \rangle$  and  $r/r_{180}$  (normalized to the average temperature, the average metallicity and the virial radius measured in each cluster, respectively, as described in Section 3) with  $r < 0.1r_{180}$  have been considered to characterize the cooling cores. We find that the most robust correlation is present between the slope  $\mu$  of the temperature profiles,

$$kT/\langle kT \rangle = A (r/r_{180})^\mu, \quad (4)$$

and  $\tau_c/\tau_{age}$ , with a Spearman's  $\rho$  rank correlation value of -0.87 that corresponds to a significance of the non-correlation case of  $P = 2 \times 10^{-4}$ . In the  $kT - Z$  and  $Z - r$  relations, the values of the Spearman's  $\rho$  are 0.44 and 0.54, corresponding to a significance of 0.15 and 0.07, respectively. The exponent  $\mu$  correlates with  $\tau_c/\tau_{age}$ , being higher at lower values of  $\tau_c/\tau_{age}$ , with all the CC clusters having  $\mu > 0$  and  $\tau_c/\tau_{age} \lesssim 0.6$  (Figure 6).

## 4. CONCLUSIONS

In the present work we analyzed a sample of 12 galaxy clusters present in the Chandra archive with at least  $\sim 20,000$  net ACIS counts and  $kT > 6$  keV. These clusters were chosen in the 0.1-0.3 redshift range, regardless of their shape. We computed the cooling time of the clusters, subdividing the sample in 7 cool core clusters and 5 non-cool core clusters. This subdivision allowed us to compare the two categories in a systematic fashion, following the approach of DM01. We performed a spectral analysis in radial bins of each cluster in the sample requiring each bin to have  $\sim 7000 - 8000$  counts, fitting the spectra with a thermal model with Galactic absorption. This allowed us to derive temperature and metallicity profiles for each cluster. The virial radius

$r_{180}$  was computed in order to renormalize the radii to physically meaningful quantities and investigate for self-similarities in the radial profiles. To this aim the global temperature  $\langle kT \rangle$  and metallicity  $\langle Z \rangle$  in each cluster were measured as well. The main results coming from our work can be summarized as follows.

- The temperature profiles in the inner  $0.1r_{180}$  have, on average, a positive gradient,  $kT(r) \propto r^\mu$  with  $\mu \simeq 0.25$  in CC systems, whereas it is almost flat in NCC systems. The outer regions are well fitted with a single power-law with slopes significantly different, being steeper ( $\mu = -0.32 \pm 0.05$ ) in NCC objects. The general trend of our CC sample is fully consistent with Vikhlinin et al. (2005) at  $r \lesssim 0.3r_{180}$ . The low number statistics above  $0.3r_{180}$  prevents us from any statistically significant comparison between the two samples at  $r \gtrsim 0.3r_{180}$ .
- The metallicity profiles in the inner regions is almost constant in NCC clusters around the value measured excluding counts from  $r < 0.07r_{180}$ . In the CC sample, a steep negative gradient is observed ( $\mu = -0.27 \pm 0.03$ ) in the central regions. At  $r > 0.1r_{180}$ , a power-law reproduces well the distribution of the spectral measurements, with a slope that is marginally steeper in CC clusters ( $\mu = -0.52 \pm 0.18$ ) than in NCC clusters ( $\mu = -0.29 \pm 0.27$ ).
- Comparing our averaged metallicity profiles with the ones in DM01, we found that our values of  $Z/\langle Z \rangle$  are systematically higher, with differences up to 50% within  $0.1r_{180}$  of CC systems. This may be explained by the different method adopted in DM01 to estimate  $\langle Z \rangle$ , as best-fit with a constant over the entire metallicity profile, without any exclusion of the central core.
- Using the solar abundances from Asplund (2005, A05) gives consistent results with what we obtain using the values by Anders & Grevesse (1989, AG89), with a discrepancy only in the normalization (as expected,  $\sim 60 - 70\%$  higher) but not in the slope of the  $Z$  radial profiles. Together with the fact that, in most cases, we were able to measure the  $\alpha$  elements only as upper limits, this indicates that our metallicities are mostly driven by Iron and that adopting the AG89 solar abundances instead of the A05 results in a difference only in the absolute values of the  $Z$  measured but does not introduce any bias in the radial profile analysis.
- Fitting a power-law shape to the temperature profiles,  $kT/\langle kT \rangle = A (r/r_{180})^\mu$ , we found that  $\mu$  correlates strongly with the cluster cooling times, being higher at low values of  $\tau_c/\tau_{age}$ , with all the CC clusters having  $\alpha > 0$  and  $\tau_c/\tau_{age} \lesssim 0.6$ . As expected, strong correlation is also observed between the inner slope of the metallicity profile and cluster cooling time.

In general, our results further demonstrate the invaluable role played by X-ray archival studies of the

chemo- and thermo-dynamical properties of galaxy clusters. Analyses based on the Chandra archive, like that presented here (see also Vikhlinin et al. 2005; Balestra et al. 2007; Maughan et al. 2007), in combination with analogous studies from the XMM-Newton archive, will constitute an important heritage from the present generation of X-ray satellites for years to come. Nowadays, available data on the evolution of the chemical enrichment of the ICM provide important constraints on models aimed at explaining the past history of star formation and the dynamical processes taking place during the cosmological build up of galaxy clusters. However the study of the thermo-dynamical properties of the cooling cores and the evolution of the abundance distributions in clusters with the redshift are just a part of what can be currently done exploiting in full the existing Chandra and XMM-Newton archives. Archival works like ours have

the potential to shed new light on the properties of the stellar populations responsible for the ICM enrichment, and on the mechanisms which lead to the generation of the cool cores and determine the transport and diffusion of heavy elements from star forming regions.

AB and PM acknowledge financial support from CXO grant AR6-7015X and from NASA grant GO5-6124X. We acknowledge financial contribution from contract ASI-INFN I/023/05/0. PT and SB acknowledge financial contribution from the PD51 INFN grant. We thank A. Vikhlinin for providing us the temperature and abundance profiles of some of the clusters in his sample. We also thank F. Gastaldello for useful discussions. We thank the anonymous referee for comments and suggestions useful to improve the presentation of the paper.

#### REFERENCES

- Anders, E., & Grevesse, N. 1989, *Geochim. Cosmochim. Acta*, 53, 197 (AG89)
- Arnaud, K. A. 1996, in *ASP Conf. Ser. 101: Astronomical Data Analysis Software and Systems V*, ed. G. H. Jacoby & J. Barnes, 17–+
- Asplund, M., Grevesse, N., & Sauval, A. J. 2005, in *ASP Conf. Ser. 336: Cosmic Abundances as Records of Stellar Evolution and Nucleosynthesis*, ed. T. G. Barnes & F. N. Bash, 25–+ (A05)
- Balestra, I., Tozzi, P., Ettori, S., Rosati, P., Borgani, S., Mainieri, V., & Norman, C., 2007, *A&A*, 462, 429
- De Grandi, S., & Molendi, S. 2001, *ApJ*, 551, 153 (DM01)
- De Grandi, S., & Molendi, S. 2002, *ApJ*, 567, 163 (DM02)
- Ettori, S., De Grandi, S., & Molendi, S. 2002, *A&A*, 391, 841
- Ettori, S., Tozzi, P., Borgani, S., & Rosati, P. 2004, *A&A*, 417, 13
- Evrard, A. E., Metzler, C. A., & Navarro, J. F. 1996, *ApJ*, 469, 494
- Finoguenov, A., David, L. P., & Ponman, T. J. 2000, *ApJ*, 544, 188
- Grevesse, N., & Sauval, A. J. 1998, *Space Science Reviews*, 85, 161
- Irwin, J. A., & Bregman, J. N. 2001, *ApJ*, 546, 150
- Kaastra, J. S. 1992, (Internal SRON-Leiden Report, updated version 2.0)
- Liedahl, D. A., Osterheld, A. L., & Goldstein, W. H. 1995, *ApJ*, 438, L115
- Machacek, M. E., Bautz, M. W., Canizares, C., Garmire, G. P. 2002, *ApJ*, 567, 188
- Majerowicz, S., Neumann, D. M., Reiprich, T. H. 2002, *A&A*, 394, 77
- Markevitch, M., et al. 2003, *ApJ*, 583, 70
- Matteucci, F., & Vettolani, G. 1988, *A&A*, 202, 21
- Maughan, B. J., Jones, C., Forman, W., & Van Speybroeck, L. 2007, *ApJ*, submitted, arXiv:astro-ph/0703156
- Nousek, J. A., & Shue, D. R. 1989, *ApJ*, 342, 1207
- Piffaretti, R., Jetzer, P., Kaastra, J. S., Tamura, T. 2005, *A&A*, 433, 101
- Pratt, G. W., & Arnaud, M. 2002, *A&A*, 394, 375
- Pratt, G. W., Böhringer, H., & Finoguenov, A. 2005, *A&A*, 433, 777
- Renzini, A. 1997, *ApJ*, 488, 35
- Rosati, P., Borgani, S., & Norman, C. 2002, *ARA&A*, 40, 539
- Stark, A. A., Gammie, C. F., Wilson, R. W., Bally, J., Linke, R. A., Heiles, C., Hurwitz, M. 1992, *ApJS*, 79, 77
- Tamura, T., Kaastra, J. S., den Herder, J. W. A., Bleeker, J. A. M., Peterson, J. R. 2004, *A&A*, 420, 135
- Vikhlinin, A., Markevitch, M., Murray, S. S., et al. 2005, *ApJ*, 628, 655
- Voigt, L. M., & Fabian, A. C. 2006, *MNRAS*, 368, 518
- Voit, G. M. 2005, *Reviews of Modern Physics*, 77, 207